

Study of the Structural and Magnetic Properties of NiZn Ferrite Nanoparticles Synthesized by Thermal Decomposition

Prabhakar Kumar¹, K. Bharath Raj², Dr. Satish Kumar³

¹Research Scholar, Mansarovar Global University, Bhopal, Madhya Pradesh, India

²Research scholar, Mansarovar Global University, Madhya Pradesh, India

³Associate Professor of Physics, Mansarovar Global University, Bhopal, Madhya Pradesh, India

ABSTRACT

Thermal decomposition was used to create $\text{Ni}_{1-x}\text{Zn}_x\text{Fe}_2\text{O}_4$ ($x = 0.6, 0.7, 0.8$) nanoparticles. It was determined that the synthesised particles were pure spinel ferrite structures and that their diameter ranged from 48 to 52 nm, depending on the composition. The particle size of the ferrite nanoparticles in the FE-SEM picture is around 50 nm, which is consistent with the result of the Scherrer equation. They have spherical forms with some mild aggregation. As the Zn concentration rose from 0.6 to 0.8, the ferrite nanoparticles' lattice parameter grew monotonically from 8.35 to 8.368. From 82.44 to 84.87 emu/g, the saturation magnetization value first progressively falls. Then, as the zinc concentration rises from $x = 0.6$ to 0.7 to 0.8 , it rapidly drops to 72.82 emu/g. By sintering ferrite nanoparticles at 1255 °C, $\text{Ni}_{1-x}\text{Zn}_x\text{Fe}_2\text{O}_4$ toroidal samples were made, and regardless of the amount of zinc present, all of them showed faceted grain morphologies with grain diameters of roughly 6 m. With increasing the zinc concentration from $x = 0.6$ through 0.7 to 0.8 , the actual magnetic permeability (μ) of the toroidal samples grew monotonically from 104 to 145 to 220. The cutoff frequency of the ferrite toroidal samples was determined to be around 20 MHz from the wide maximum point, according to the imaginary magnetic permeability (μ') vs. frequencies plot, which looked to be connected to domain wall resonance.

Keywords: Paramagnetic, NiZn Ferrite, Spinel Ferrite, Nanoparticles

INTRODUCTION

Based on their high resistivity and low loss at high frequencies, spinel ferrite nanoparticles like NiZn and MnZn have attracted a lot of attention for a variety of applications [1,2,3] such as high frequency circuits, the cores of radiofrequency (RF) transformers, inductors, antennas, and radar absorbing materials. Additionally, they hold considerable promise as effective catalysts and/or catalytic supports for the oxidation of organic or inorganic contaminants [1]. By utilising their suitable magnetic properties, antimicrobial activity, and biological compatibility, NiZn ferrite nanoparticles are becoming more and more significant in the field of bio-medical applications, such as magnetic resonance imaging (MRI), drug delivery systems, and hyperthermia treatment of cancer [8,9]. Figure 1 demonstrates the spinel structure, which has a cubic closed-packing of O_2 ions and is made up of 24 cations (Zn^{2+} , Fe^{2+} , Co^{2+} , Mn^{2+} , Mg^{2+} , and Ni^{2+}) and 32 O_2 anions [5,18]. It typically has a chemical form of AB_2O_4 . The smaller octahedral interstitial B site is shown by the square brackets, whereas the bigger tetrahedral interstitial A site is indicated by the round brackets. Zinc ferrite is referred to as a typical spinel structure with the formula ZnFe_2O_4 with Zn^{2+} and Fe^{3+} ions occupying the tetrahedral and octahedral positions, respectively.

The structure of nickel ferrite, FeNiFeO_4 , is referred to as an inverse spinel, with half of the Fe^{3+} ions occupying the tetrahedral sites and the other half the octahedral sites. NiZn ferrite, also known as $\text{Zn}_x\text{Fe}_{(1-x)}\text{Ni}_{(1-x)}\text{Fe}_{(1+x)}\text{O}_4$, is a kind of solid solution made up of Ni ferrite and Zn ferrite. The quantity of 3d unpaired electrons in transition metals has a significant impact on the magnetic characteristics of the NiZn ferrite. While Ni^{2+} ions have two unpaired electrons and Fe^{2+} ions have five unpaired electrons in their 3d orbitals, Zn^{2+} ions do not have any unpaired electrons in theirs. Since the addition of transition metal ions causes some Fe^{3+} ions to move from the octahedral sites to the tetrahedral sites, the unequal distribution of Fe^{3+} ions in both lattice sites effectively produces the remaining unpaired electrons, the proper loading of the Ni^{2+} ion, which has unpaired electrons, into the crystal structure of ZnFe_2O_4 results in much better magnetic properties, such as higher saturation magnetization (M_s).

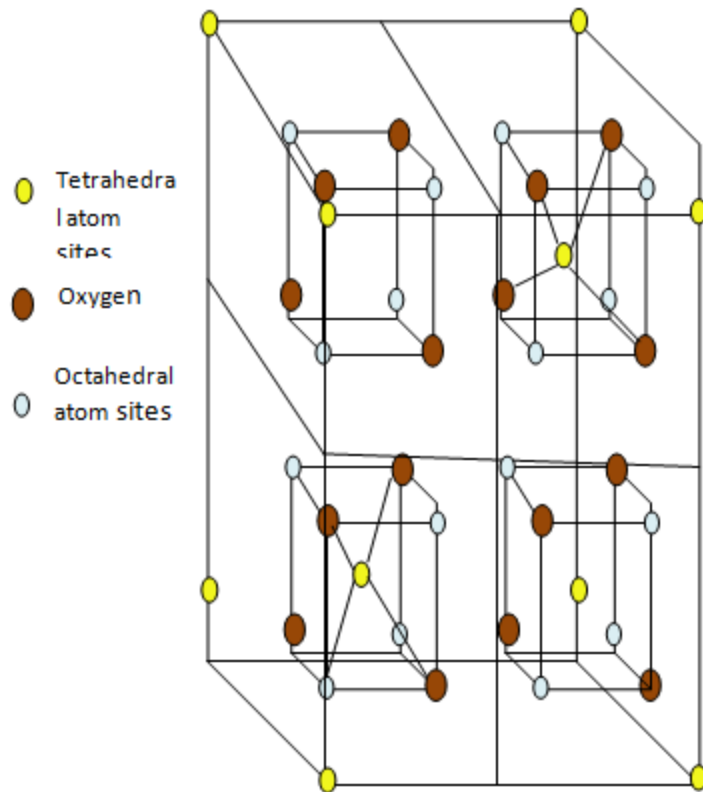


Fig. 1: The tetrahedral and octahedral structures of ferrites are indicated by the spinel structure.

In general, as the particle size is decreased, the coercive force rises gradually until it reaches its maximum value. However, if the particle size is decreased to a critical size, the thermal effect intensifies and results in super paramagnetic properties, where each particle transforms into a single domain with extremely low magnetic loss and high magnetic permeability [15]. Controlling the particle size is crucial since the characteristics of the nanocrystals significantly depend on it and the superparamagnetic particles have low coercive force and high magnetism. The synthesis technique and its preparation conditions have a significant impact on the properties of NiZn ferrite nanoparticles. Magnetic nanoparticles' shape and composition greatly affect the magnetic properties of both their individual particles as well as bulk samples following sintering. According to the relationship of $\mu = M_s D / K_1$, where $K_1 = M_s H_c / 0.96$ is the crystalline anisotropy constant, M_s is the saturation magnetization, H_c is the coercivity, and D is the average grain size, the initial permeability of magnetic nanoparticles generally increases as their saturation magnetization rises.

Sol-gel, co-precipitation, high energy ball milling, thermal breakdown, and other processes may all be used to create ferrite nanoparticles [12,14]. The thermal breakdown approach offers greater benefits than other methods for producing consistent, small, and highly crystalline nanoparticles. Additionally, this approach makes it simple to regulate particle size and particle size distribution [25,30]. There are, however, just a few studies that demonstrate the link between the permeabilities of sintered magnetic samples and their magnetization values and provide detailed explanations of the association. Therefore, understanding and enhancing magnetic characteristics may be facilitated by researching NiZn ferrite systems that exhibit these magnetic behavioural correlations.

In this study, we synthesized $Ni_{1-x}Zn_xFe_2O_4$ ($x = 0.6, 0.7, 0.8$) nanoparticles by thermal decomposition and investigated the effects of the Ni/Zn ratio on the crystal structures, microstructures, and magnetic properties of the NiZn ferrites using an X-ray diffractometer (XRD), a field emission scanning electron microscope (FE-SEM), vibrating sample magnetometer and an impedance analyzer.

MATERIALS AND METHODS

Figure 2 illustrates the thermal breakdown process used to create $Ni_{1-x}Zn_xFe_2O_4$ ($x = 0.6, 0.7, 0.8$) nanoparticles. Iron(III) acetylacetonate (96%), zinc acetylacetonate hydrate (95%), and nickel(II) acetylacetonate (96%) were the raw ingredients.

Oleic acid (90%) and oleylamine (70%), 1,2-hexadecandiol (90%) and benzyl ether (97%) were utilised as surfactants, reducing agents, and solvents, respectively. Ni, Zn and Fe-acetylacetonate precursors were weighed, respectively according to the chemical form of $Ni_{1-x}Zn_xFe_2O_4$ ($x = 0.6, 0.7, 0.8$) and poured into a 500 ml three neck flask that was filled with a mixed solution of 6 mmol oleic acid, 6 mmol oleylamine, 1,2-hexadecandiol, and 20 ml benzyl ether.

The precursor solution was heated to 200°C for one hour, then held at that temperature for one hour while being refluxed with cooling water. The procedure was carried out in a N₂ environment. The reaction product was cooled to room temperature, centrifuged at 4000 rpm for 30 minutes, then repeatedly washed with hexane and ethanol to remove the organic residue from the ferrite particles. Oleic acid and oleylamine were among the fat acids that hexane was employed to dissolve. $Ni_{1-x}Zn_xFe_2O_4$ ($x = 0.6, 0.7, 0.8$) nanoparticles were then collected and dried at 100°C for 24 hours. Uniaxial pressing was used to create NiZn ferrites toroidal samples. To create green toroidal samples, the ferrite powder was combined with a PVA (Polyvinyl alcohol, 5 weight percent) binder solution. This mixture was then put into a toroidal-shaped mould and subjected to pressure of 1 toncm⁻². The green toroidal samples were sintered at 1250°C for two hours after being burnt off at 650°C for 30 minutes in the air.

An X-ray diffractometer was used to examine the phase purity of the NiZn ferrites nanoparticles. A scanning electron microscope (SEM) was used to examine the microstructures of sintered toroidal ferrite samples. From 1 MHz to 1 GHz, magnetic permeability (μ, μ') was determined using an impedance analyzer. A vibrating sample magnetometer (VSM) was used to assess the ferrite particles saturation magnetization.

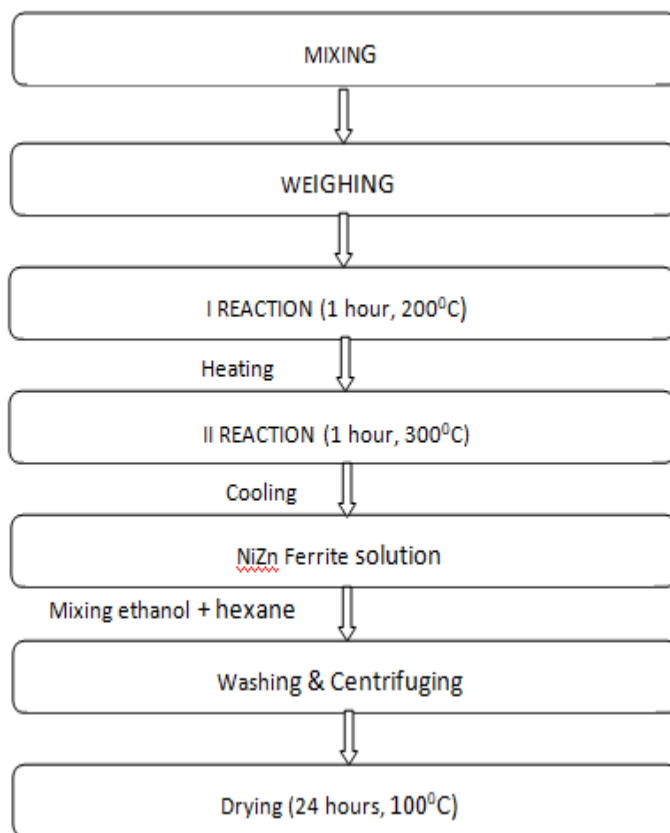


Fig.2. The Experimental Process For Synthesizing $Ni_{1-x}Zn_xFe_2O_4$ ($x = 0.6, 0.7, 0.8$) Nanoparticles

RESULTS

Figure 3 depicts the X-ray diffraction patterns of $Ni_{1-x}Zn_xFe_2O_4$ ($x = 0.6, 0.7, 0.8$) nanoparticles, which, independent of the composition, reveal a pure spinel structure for all three ferrites without any second phases. The following equation was used to compute the ferrite nanoparticles' lattice properties, which are shown in Figure 4 as a function of the Ni concentration.

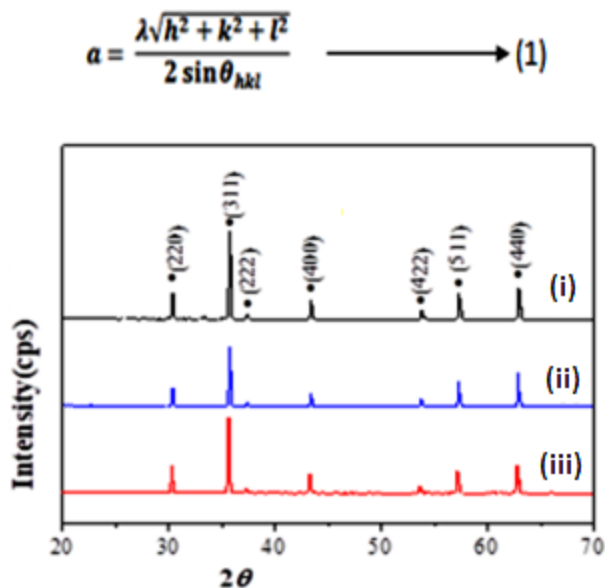


Figure 3. X-ray diffraction patterns of $\text{Ni}_{1-x}\text{Zn}_x\text{Fe}_2\text{O}_4$ ($x = 0.6, 0.7, 0.8$) nanoparticles of the synthesized samples (i) $x = 0.6$, (ii) $x = 0.7$ and (iii) $x = 0.8$

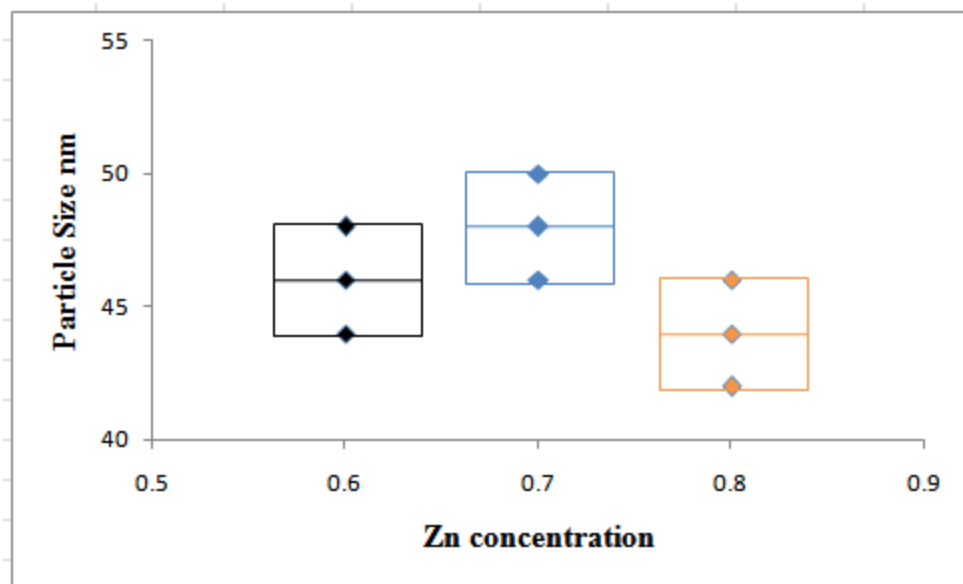


Figure 4. The dependence of the crystallite size of $\text{Ni}_{1-x}\text{Zn}_x\text{Fe}_2\text{O}_4$ ($x = 0.6, 0.7, 0.8$) ferrite nanoparticles on the Zn concentration

Due to the Zn^{2+} ion's greater ionic radius (0.74\AA) than the Ni^{2+} ion (0.69\AA), which increases monotonically with increasing Zn concentration from $x = 0.6$ to 0.8 , the lattice parameter rises from 8.345 to 8.362 . Given that the larger Zn^{2+} ions prefer tetrahedral A-sites whereas the smaller Ni^{2+} ions prefer octahedral B-sites in the crystalline spinel structure, this data indicates that some Zn ions appear to be integrated into Ni sites. Since their ionic radii differ, it makes sense that the lattice volume of $\text{Ni}_{1-x}\text{Zn}_x\text{Fe}_2\text{O}_4$ grew with rising Zn concentration. Figure 5 illustrates the relationship between the size of ferrite nanoparticle crystallites and the Zn concentration. The average crystallite size (D) was determined from the (311) peak using Scherer's equation, as stated below.

$$D = \frac{k\lambda}{\beta \cos \theta} \longrightarrow (2)$$

where β is the full width half maximum of the (311) diffraction peak, $k = 0.89$, and $\lambda = 1.5406 \text{ \AA}$. The crystallite size was in the range of 45 to 52 nm and did not change much depending on the Zn content. The hysteresis curve of NiZn ferrite nanoparticles at ambient temperature is shown in Figure 6. $\text{Ni}_{1-x}\text{Zn}_x\text{Fe}_2\text{O}_4$, saturation magnetization and coercivity decline from 83 to 71 emu/gm and from 18.54 to 16.48 Oersted, respectively, when the Zn ion concentration rises from $x = 0.6$ to 0.8, which is high in comparison to some other values. The $\text{Ni}_{1-x}\text{Zn}_x\text{Fe}_2\text{O}_4$'s magnetic characteristics rely on its chemical makeup, grain size, manufacturing technique, and cation arrangement between two interstitial sites [28]. Domain wall motion and magnetization rotation inside domains are the two magnetization processes that the ferrite experiences when an applied field is present. In general, extrinsic material characteristics including grain size and grain-boundary structure, the existence of inclusions or holes inside grains, impurity levels, and pressures have an impact on domain wall motion. Given that the crystallite size acquired from the XRD is nearly identical to the particle size obtained from the FE-SEM picture, Figure 7 demonstrates that the $\text{Ni}_{1-x}\text{Zn}_x\text{Fe}_2\text{O}_4$ particles are regarded single domain particles. Therefore, it would seem that the cation arrangement on the sub-lattices A and B is what is primarily responsible for the high saturation magnetization. The fact that the Curie temperature, which denotes the temperature at which the paramagnetic and ferromagnetic phases change, quickly drops with increasing nonmagnetic Zn ions in NiZn ferrite [29] is in good agreement with the reduction in saturation magnetization with Zn ion concentration.

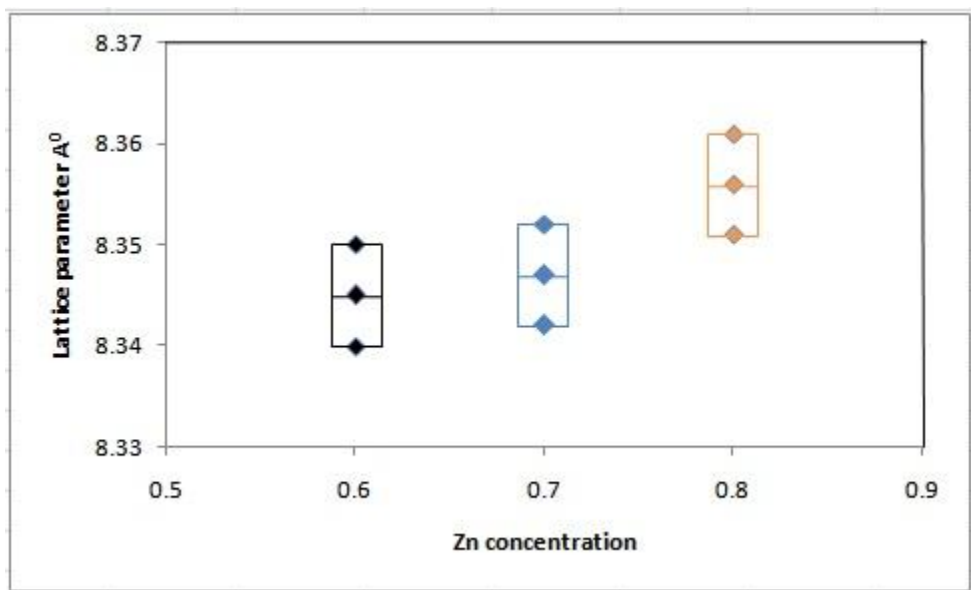


Figure 5: The dependence of the lattice parameters of the $\text{Ni}_{1-x}\text{Zn}_x\text{Fe}_2\text{O}_4$ ($x=0.6, 0.7, 0.8$) ferrite nanoparticles on the Zn concentration

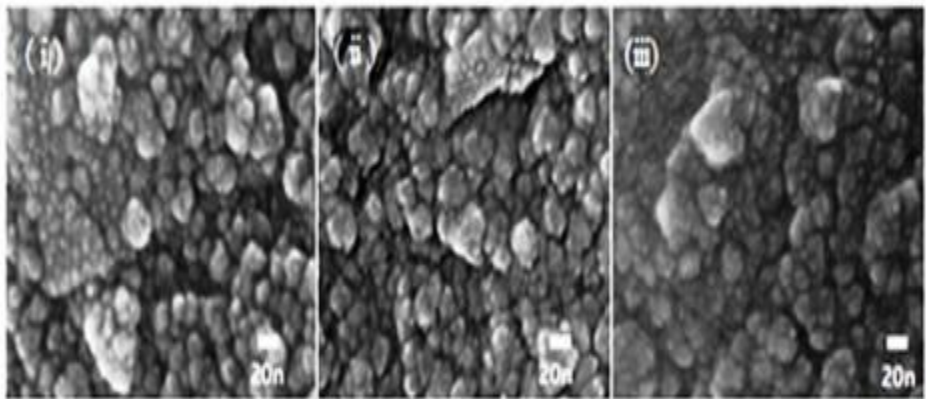


Figure 6. FE-SEM image of synthesized $\text{Ni}_{1-x}\text{Zn}_x\text{Fe}_2\text{O}_4$ ($x=0.6, 0.7, 0.8$) nanoparticles

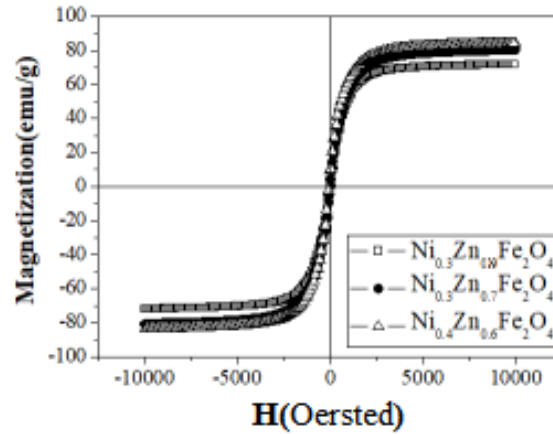


Figure 7. Hysteresis curves of $Ni_{1-x}Zn_xFe_2O_4$ ($x=0.6, 0.7, 0.8$) nanoparticles

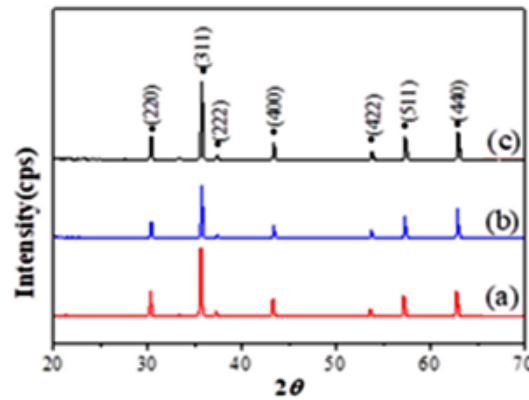


Figure 8. The X-ray diffraction patterns of the $Ni_{1-x}Zn_xFe_2O_4$ ($x = 0.6, 0.7, 0.8$) samples sintered at $1250^{\circ}C$

The X-ray diffraction patterns of the $Ni_{1-x}Zn_xFe_2O_4$ ($x = 0.6, 0.7, 0.8$) samples sintered at $1250^{\circ}C$ are displayed in Figure 8. These X-ray diffraction patterns show no second phases, indicating that the sintered samples have the same pure spinel structure independent of their chemical composition. The sintered samples all contain the same pure spinel structure. Figure 10 shows FE-SEM images of $Ni_{1-x}Zn_xFe_2O_4$ sintered at $1250^{\circ}C$ ($x = 0.6, 0.7, \text{ and } 0.8$). In $Ni_{1-x}Zn_xFe_2O_4$ ferrite, it should be noted that the microstructures get denser as the Zn concentration rises. According to the research, Zn ions not only reduce the sintering temperature but also significantly contribute to raising the sintering density. This behaviour is consistent with that finding. The particle shape is faceted, which is fascinating to remark given that the particle size is rather constant at $5\mu m$.

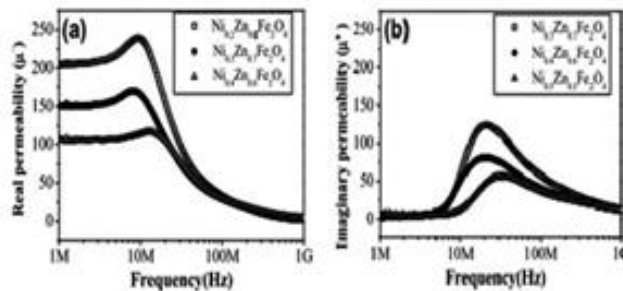


Figure 9 Real part (a) and Imaginary part (b) of the magnetic permeability of $Ni_{1-x}Zn_xFe_2O_4$ ($x=0.6, 0.7, 0.8$) in the frequency range 1 MHz to 1 GHz

The magnetic permeability of $Ni_{1-x}Zn_xFe_2O_4$ toroidal samples is shown in Figure 9 for the frequency range of 1 MHz to 1 GHz as real and imaginary components. As demonstrated in Figure 9, the real permeability (μ) at 5 MHz increases monotonically with increasing Zn concentration from $x = 0.6$ to 0.8 in of $NiZnFe_2O_4$ from $\mu = 106$ to 217 . The value of μ is consistent for all three toroid samples up to 10 MHz and steadily increases with frequency. The imaginary portion of permeability (μ') rises with frequency and reaches a wide maximum at 20 MHz, where falls off quickly. Domain wall resonance, which comprises of relaxation and resonance type dispersions, leads to this property. Thus, the complicated permeability spectrum of domain wall motion in the low frequency domain may be seen as the superposition of resonance and relaxation dispersion [25]. The overlap of the spin resonance and domain wall motion resonance is what causes the wide maximum in [30–33]. Only the spin rotational component becomes prominent at higher frequencies, and the effects of domain wall motion on the complex permeability spectrum steadily decrease [35]. Domain wall resonance is the primary ferrite magnetizing mechanism below 500 kHz, whereas rotational resonance [32,33] and domain wall resonance [35] occur beyond 1 GHz.

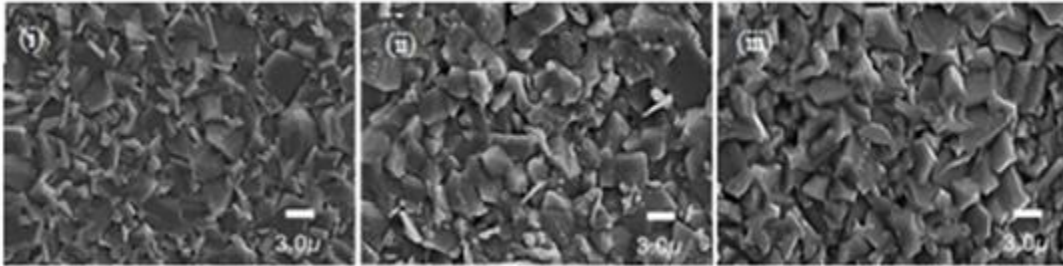


Figure 10 FE-SEM images of the $Ni_{1-x}Zn_xFe_2O_4(x=0.6, 0.7, 0.8)$ samples sintered at $1250^{\circ}C$

The difference in sub-lattice magnetism linked to the octahedral and tetrahedral sites determines the saturation magnetization of ferrite. Tetrahedral sites in regular spinel are inhabited by divalent cations, but in reverse spinel, trivalent cations fill these sites. $NiFe_2O_4$ is inverse spinel, whereas $ZnFe_2O_4$ is said to be normal spinel. $Ni_{1-x}Zn_xFe_2O_4$ is created when $ZnFe_2O_4$ and $NiFe_2O_4$ are combined. With an increase in Zn concentration, Zn^{2+} cations replace Fe^{3+} in the tetrahedral positions, while Fe^{3+} fills the octahedral sites that Ni^{2+} had previously occupied. There are no unpaired electrons in the Zn^{2+} ion, however there are two in the Ni^{2+} ion and five in the Fe^{3+} ion. The octahedral and tetrahedral sites of ferrite have been defined according to the following convention: $Zn^{2+}(Fe^{3+})_4$ with the ions on the octahedral sites enclosed in brackets, O_4 normal spinel $Fe^{3+}(Ni^{2+}Fe^{3+})_4$ is an inverse spinel. In accordance with the various cations available, ferric ions may occupy tetrahedral or octahedral sites. Since ferric ions have a less affinity for the tetrahedral site than non-magnetic Zn ions do, the number of Fe^{3+} ions on the tetragonal A-site will decrease when non-magnetic Zn ions are integrated into the $NiFe_2O_4$ lattice. Equation (4) describes the relationship between the net magnetic moment in nickel zinc ferrite and the quantity of unpaired electrons. The number of unpaired electrons in nickel zinc ferrite is proportional to Equation (4), while the Zn^{2+} ions have no unpaired electrons while the Ni^{2+} ions have two. The Fe^{3+} ions have five unpaired electrons, compared to two unpaired electrons for the Ni^{2+} ions and none for the Zn^{2+} ions [30]. According to equations 3 and 4, saturation magnetization is thought to rise as the content increases.



$$M = -0(y) - 5(1-y) + 2(1-y) + 5(1+y) = 2 + 8y \quad \text{----- (4)}$$

Where y represents the percentage of Zn^{2+} ions in a mole. The magnetization results, which show a declining trend with rising Zn concentration, did not match the predicted value of this magnetization. However, it has been shown that when the Zn concentration in $NiZn$ ferrite grows over 0.5 mole fraction, the magnetization of the material falls [31]. Fe^{3+} ions in the tetragonal sites became so diluted at high zinc substitution levels that the super-exchange connection between the tetrahedral and octahedral sites was lost, and the saturation magnetization decreased. With increasing Zn concentration, the Curie temperature lowers sharply and finally falls below room temperature, when the magnetic characteristics vanish.

CONCLUSION

Thermal decomposition method was used to successfully synthesize $Ni_{1-x}Zn_xFe_2O_4(x = 0.6, 0.7, 0.8)$ nanoparticles, and X-ray diffraction examination confirmed that they were pure spinel ferrite structures. The Scherrer equation estimated the diameter of the synthesised ferrite nanoparticles to be between 45 and 50 nm, which was in agreement with the particle size of around 50 nm shown in FE-SEM pictures. As the Zn level rose, the ferrite nanoparticles' lattice parameters rose

monotonically. Depending on their composition, the synthesised ferrite nanoparticles had reasonably high saturation magnetization values of 72–81 emu/g. Toroidal samples with a grain size of around 5 μ m were created by sintering ferrite nanoparticles at 1250 $^{\circ}$ C. These samples showed faceted grain morphology in FE-SEM pictures. With increasing Zn concentration, the toroidal sample's actual magnetic permeability (μ), as measured at 5 MHz, rises and showing $\mu = 217$ for $x = 0.7$. About 20 MHz was the cutoff frequency of the ferrite toroidal sample, which appeared to be related to domain wall resonance.

REFERENCES

- [1]. Shangguan, W.F.; Teraoka, Y.; Kagaw, S. Promotion effect of potassium on the catalytic property of CuFe₂O₄ for the simultaneous removal of NO_x and diesel soot particulate. *Appl. Catal. B Environ.* 1998, 16, 149.
- [2]. Han, D.H.; Luo, H.I.; Yang, Z. Remanent and anisotropic switching field distribution of platelike Ba-ferrite and acicular particulate recording media. *J. Magn. Magn. Mater.* 1996, 161, 376.
- [3]. Cui, H.-J.; Shi, J.-W.; Yuan, B.; Fu, M.-L. Synthesis of porous magnetic ferrite nanowires containing Mn and their application in water treatment. *J. Mater. Chem. A* 2013, 1, 5902.
- [4]. Costa, A.C.F.M.; Morelli, M.R.; Kiminami, R.H.G.A. Microstructure and magnetic properties of Ni(1-x)Z_xFe₂O₄ synthesized by combustion reaction. *J. Mater. Sci.* 2007, 42, 779.
- [5]. Carta, D.; Loche, D.; Mountjoy, G.; Navarra, G.; Corrias, A. NiFe₂O₄ Nanoparticles Dispersed in an Aerogel Silica Matrix: An X-ray Absorption Study. *J. Phys. Chem. C* 2008, 112, 15623–15630.
- [6]. Gubbala, S.; Nathani, H.; Koziol, K.; Misra, R.D.K. Magnetic properties of nanocrystalline Ni–Zn, Zn–Mn, and Ni–Mn ferrites synthesized by reverse micelle technique. *Phys. B Condens. Mater.* 2004, 348, 317.
- [7]. Goldman, M.; DeVitre, R.; Tenca, J. Materials Science Cement Distribution and Bond Strength in Cemented Posts. *J. Dent. Res.* 1984, 63, 582.
- [8]. Nowicka, A.; Kowalczyk, A.; Donten, M.; Kryszynski, P.; Stojek, Z. Influence of a Magnetic Nanoparticle as a Drug Carrier on the Activity of Anticancer Drugs: Interactions of Double Stranded DNA and Doxorubicin Modified with a Carrier. *Anal. Chem.* 2009, 81, 7474–7483.
- [9]. Sunkara, B.; Misra, R. Enhanced antibactericidal function of W⁴⁺-doped titania-coated nickel ferrite composite nanoparticles: A biomaterial system. *Acta Biomater.* 2008, 4, 273–283.
- [10]. Yaun, T.; Wei, Z.; Yuan, J.; Yan, L.; Liu, Q.; Wang, J. The microstructure and magnetic properties of Ni_{0.4}Zn_{0.6}Fe₂O₄ films prepared by spin-coating method. *J. Sol-Gel Sci. Technol.* 2011, 58, 501.
- [11]. Rameshbabu, R.; Ramesh, R.; Kanagesan, S.; Karthigeyan, A.; Ponnusamy, S. Synthesis of super paramagnetic ZnFe₂O₄ nanoparticle by surfactant assisted hydrothermal method. *J. Mater. Sci. Mater. Electron.* 2013, 24, 4279–4283.
- [12]. Rostamnejadi, A.; Salamati, H.; Kameli, P.; Ahmadvand, H. Superparamagnetic behavior of La_{0.67}Sr_{0.33}MnO₃ nanoparticles prepared via sol–gel method. *J. Magn. Magn. Mater.* 2009, 321, 3126–3131.
- [13]. Nakashima, S.; Fujita, K.; Tanaka, K.; Hirao, K.; Yamamoto, T.; Tanaka, I. First-principles XANES simulations of spinel zinc ferrite with a disordered cation distribution. *Phys. Rev. B* 2007, 75.
- [14]. Zheng, Z.; Zhong, X.; Zhang, Y.; Yu, H.; Zeng, D. Synthesis, structure and magnetic properties of nanocrystalline Zn_xMn_{1-x}Fe₂O₄ prepared by ball milling. *J. Alloy. Compd.* 2008, 466, 377–382.
- [15]. Hasirci, C.; Karaagac, O.; Köçkar, H. Super paramagnetic zinc ferrite: A correlation between high magnetizations and nanoparticle sizes as a function of reaction time via hydrothermal process. *J. Magn. Magn. Mater.* 2019, 474, 282–286.
- [16]. Byun, T.Y.; Bycon, S.C.; Hong, K.S. Factors affecting initial permeability of Co-substituted Ni-Zn-Cu ferrites. *IEEE Trans. Magn.* 1999, 35, 3445.
- [17]. Cullity, B.D.; Graham, C.D. *Introduction to Magnetic Materials*, 2nd ed.; John Wiley & Sons Inc.: New York, NY, USA, 2009.
- [18]. Kaur, B.; Arora, M.; Shankar, A.; Srivastava, A.K.; Pan, R.P. Induced Size Effects of Gd³⁺ ions Doping on Structural and Magnetic Properties of Ni-Zn Ferrite Nanoparticles. *Adv. Mater. Lett.* 2012, 3, 399–405.
- [19]. Goswami, P.P.; Choudhury, H.A.; Chakma, S.; Moholkar, V.S. Sonochemical Synthesis and Characterization of Manganese Ferrite Nanoparticles. *Ind. Eng. Chem. Res.* 2013, 52, 17848–17855. 13. Silva, F.G.D.; Depeyrot, J.; Campos, A.F.C.; Aquino, R.; Fiorani, D.D. PeddisStructural and magnetic properties of spinel ferrite nanoparticles. *J. Nanosci. Nanotechnol.* 2019, 19, 4888–4902.
- [20]. Akhtar, M.J.; Nadeem, M.; Javaid, S.; Atif, M. Cation distribution in nanocrystalline ZnFe₂O₄ investigated using X-ray absorption fine structure spectroscopy. *J. Phys. Condens. Matter* 2009, 21, 405303.
- [21]. Singh, A.K.; Goel, T.C.; Mendiratta, R.G. Low-temperature synthesis of Mn_{0.2}Ni_{0.2}Zn_{0.6}Fe₂O₄ ferrites by citrate precursor method and study of their properties. *Phys. Status Solidi (a)* 2004, 201, 1453–1457.

- [22]. Slatineanu, T.; Jordan, A.; Palamaru, M.N.; Caltun, O.F.; Gafton, V.; Leontie, L. Synthesis and characterization of nanocrystalline Zn ferrites substituted with Ni. *Mater. Res. Bull.* 2011, 46, 1455–1460.
- [23]. Pujar, R.B.; Kulkarni, S.N.; Bellad, C.B.; Chougule, B.K. Compositional, temperature and frequency dependence of initial permeability in Zr⁴⁺ substituted Mg–Zn ferrites. *J. Mater. Sci. Lett.* 1997, 16, 1668–1699.
- [24]. Kozlov, D.A.; Shcherbakov, A.B.; Kozlova, T.O.; Angelov, B.; Kopitsa, G.P.; Garshev, A.V.; Baranchikov, A.E.; Ivanova, O.S.; Ivanov, V.K. Photochromic and Photocatalytic Properties of Ultra-Small PVP-Stabilized WO₃ Nanoparticles. *Molecules* 2019, 25, 154
- [25]. Guyot, M.; Globus, A. Wall displacement and bulgingin magnetization mechanisms of the hysteresis loop. *Phys. Status Solidi B* 1972, 52, 427.
- [26]. Gao, R.-R.; Zhang, Y.; Yu, W.; Xiong, R.; Shi, J. Superparamagnetism and spin-glass like state for the MnFe₂O₄ nano-particles synthesized by the thermal decomposition method. *J. Magn. Magn. Mater.* 2012, 324, 2534–2538.
- [27]. Padmapriya, G.; Manikandan, A.; Krishnasamy, V.; Jaganathan, S.K.; Antony, S.A. Spinel Ni_xZn_{1-x}Fe₂O₄ (0.0 ≤ x ≤ 1.0) nano-photocatalysts: Synthesis, characterization and photocatalytic degradation of methylene blue dye. *J. Mol. Struct.* 2016, 1119, 39–47.
- [28]. Velmurugana, K.; Venkatachalapathyb, V.S.K.; Sendhilnathanc, S. Thermogravimetric and Magnetic Properties of Ni_{1-x}Zn_xFe₂O₄ Nanoparticles Synthesized by Coprecipitation. *Mater. Res.* 2009, 12, 529–534.
- [29]. Verma, A.; Goel, T.; Mendiratta, R.; Alam, M. Dielectric properties of NiZn ferrites prepared by the citrate precursor method. *Mater. Sci. Eng. B* 1999, 60, 156–162. [CrossRef] 30. Stoner, E.C. *Introduction to Magnetic Materials*; Addison-Wesley: Boston, MA, USA, 1972; pp. 183–187.
- [30]. Gubanova, N.; Baranchikov, A.E.; Kopitsa, G.P.; Almasy, L.; Angelov, B.; Ivanov, V.K.; Rosta, L.; Ivanov, V.K. Combined SANS and SAXS study of the action of ultrasound on the structure of amorphous zirconia gels. *Ultrason. Sonochem.* 2015, 24, 230–237.
- [31]. Tsutaoka, T. Frequency dispersion of complex permeability in Mn–Zn and Ni–Zn spinel ferrites and their composite materials. *J. Appl. Phys.* 2003, 93, 2789–2796.
- [32]. Guillaud, C. *Proprietes Manetiques des Ferrites*. *J. Phys. Radium* 1951, 12, 239–248.
- [33]. Verma, A.; Chatterjee, R. Effect of zinc concentration on the structural, electrical and magnetic properties of mixed Mn–Zn and Ni–Zn ferrites synthesized by the citrate precursor technique. *J. Magn. Magn. Mater.* 2006, 306, 313–320.
- [34]. Shaikh, P.A.; Kambale, R.C.; Rao, A.V.; Kolekar, Y.D. Effect of Ni doping on structural and magnetic properties of Co_{1-x}Ni_xFe_{1.9}Mn_{0.1}O₄. *J. Magn. Magn. Mater.* 2010, 322, 718.